Supplemental Material for "Modeling Elevated Concentrations of Organic Acids at Whiteface Mountain"

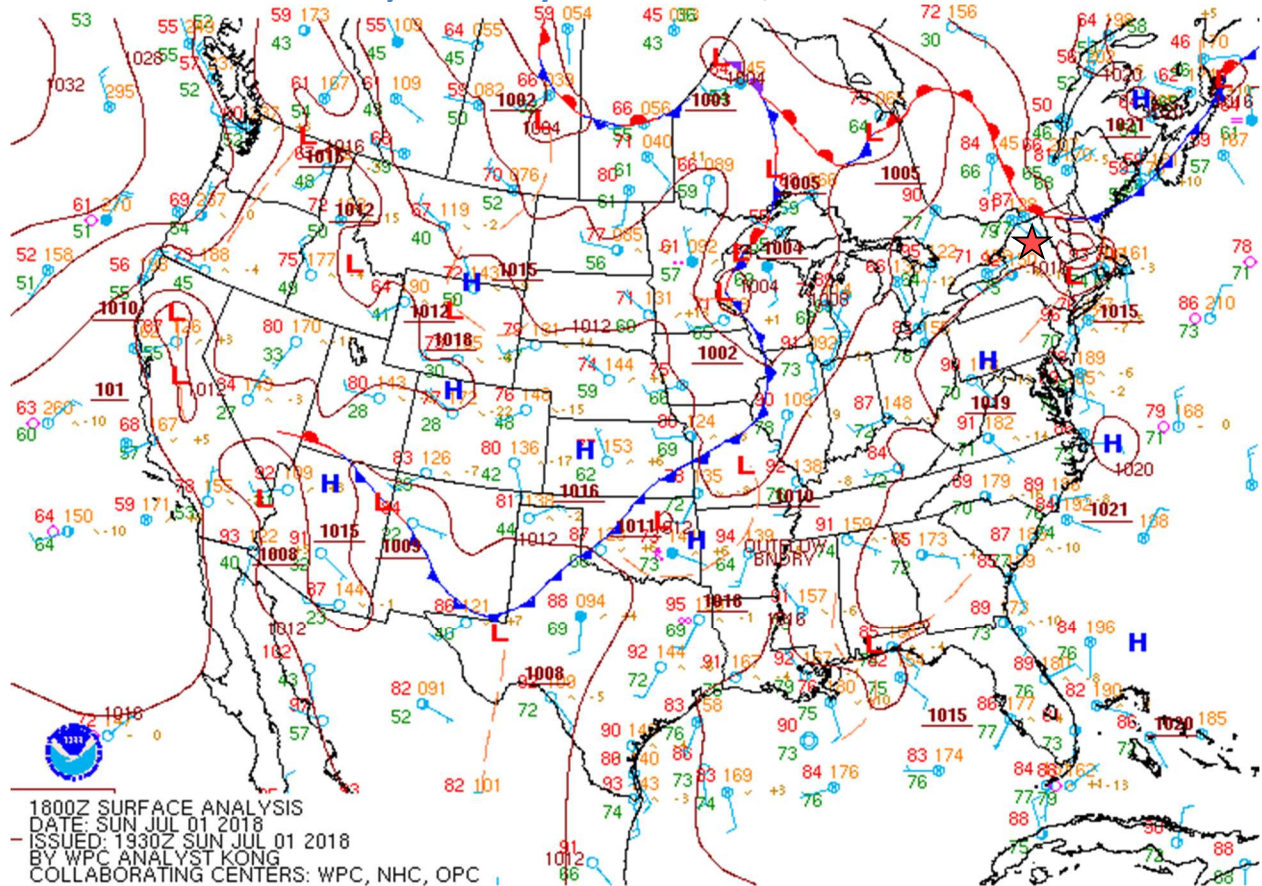## Section S1. Surface Analysis on July 1st 18:00 UTC, 2018

Figure S1. National Weather Service surface analysis showing fronts, mean sea level pressure, and station observations valid at 18:00 UTC on July 1st, 2018. The red star represents the location of Whiteface Mountain

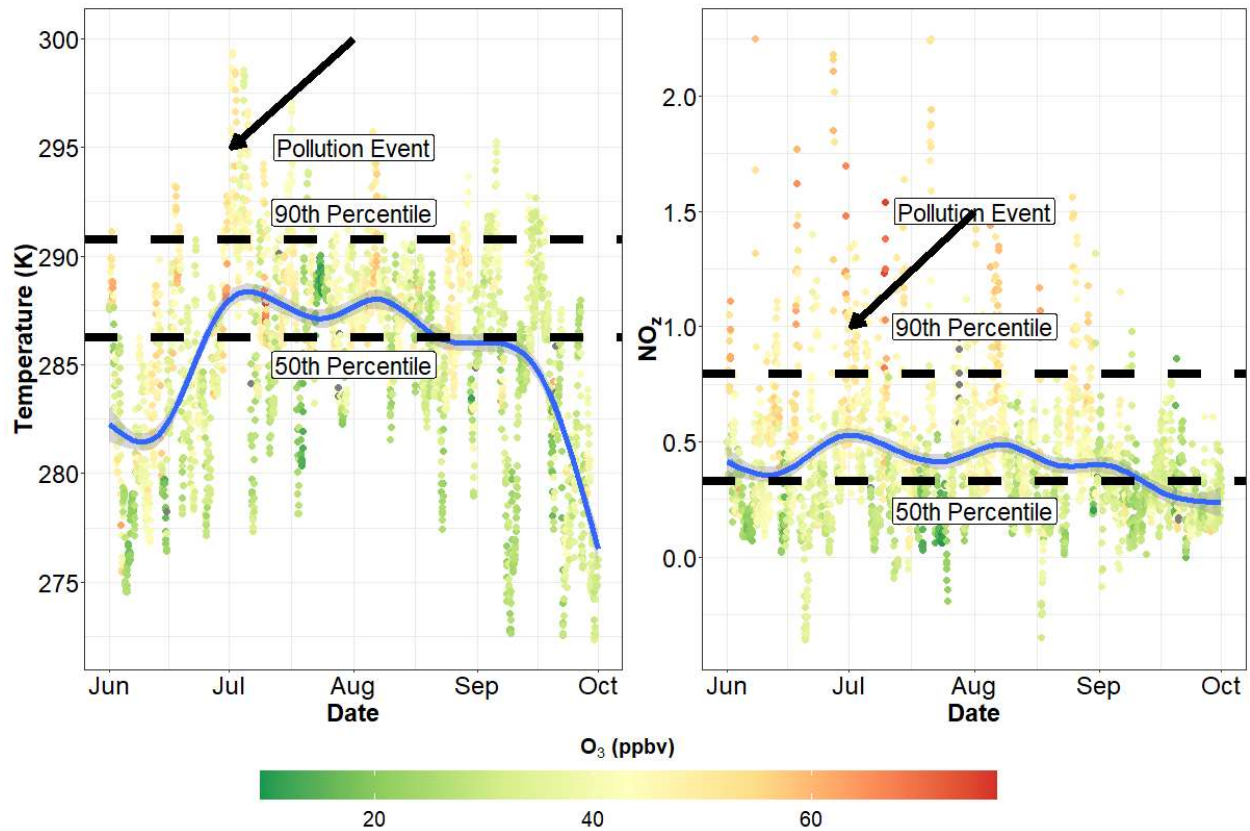## Section S3. Observations at Whiteface Mountain

Figure S2. a.) Temperature and b.) NO$_z$ mixing ratios colored by O$_3$, measured at the summit of WFM. The horizontal lines represent the 50th and 90th percentile values of a) Temperature and b) NO$_2$ mixing ratios for June-September, 2018. The blue lines represent smoothed averages using a generalized additive model.

Section S2. WRF-Chem Description

Our study uses the Weather Research and Forecasting model (Skamarock et al., 2021) coupled with Chemistry (Grell et al., 2005; Fast et al., 2006) (WRF-Chem) version 4.0.3 to simulate the air pollution event and monitor constituents and meteorological information along forward trajectories. Simulations were conducted between June 27, 2018, 00:00 UTC and July 2, 2018, at 12:00 UTC. The model domain covered the conterminous US extending into Canada (Fig. S2) with horizontal grid resolution at 12 km x 12 km, and 43 vertical layers ranging from the surface to 50 hPa.
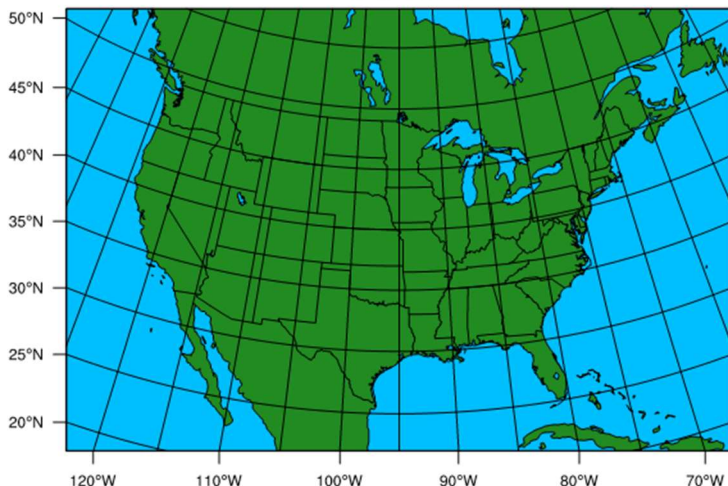
Figure S3. The model domain used for WRF-Chem simulation

The prognostic variables including winds, potential temperature, pressure, water vapor, condensed water (i.e., cloud particles), tracer variables, trace gases, and aerosols, are integrated forward in time using a Runge-Kutta integration method. The moisture variables, scalars, and chemistry species are advected using a positive definite and monotonic scheme (Wang et al., 2009). Meteorological conditions are initialized using the Global Forecast System Final Analysis data (GFS-FNL), while chemical species are initialized from the Whole Atmosphere Community Climate Model. WRF's observational nudging data assimilation (OBSGRID) tool is applied to reduce the meteorological error and allow for the focus on chemistry. For the nudging, observational data are from the NOAA Meteorological Assimilation Data Ingest System (MADIS). The meteorological measurements used in the WRF simulation are the Integrated Mesonet Dataset and the NWS radiosonde data. The OBSGRID nudging improved the WRF simulation every 3 hours by adjusting free troposphere moisture and winds.

Gas phase chemistry is represented by the MOZART 4 chemistry scheme (Emmons et al., 2010), updated to contain detailed chemistry to represent isoprene, monoterpene, aromatics, methyl butanol (or more fully, 2-methyl-3-buten-2-ol), nitrous acid, and ethene, while also containing updated isoprene chemistry (Knote et al 2014). The gas-phase chemistry solved the stiff set of gas phase differential equations using a Rosenbrock solver (Sandu and Sander, 2006). Aerosols are modeled using the MOSAIC aerosol module using the volatility basis set described in Lane et al., 2008, and updated by Knote et al., 2014. This scheme predicts both the organic and inorganic composition of aerosol in 4 size bins (Bin 01: 0.039-0.156 μm diameter; Bin 02: 0.156-0.625 μm diameter; Bin 03: 0.625-2.5 μm diameter; Bin 04: 2.5-10. μm diameter). Inorganic chemistry is controlled by the Multicomponent Equilibrium Solver for Aerosols (MESA) thermodynamic model (Zaveri et al., 2008). Primary organic aerosols are assumed to be inert, meaning that evaporation or the subsequent oxidation of vaporized organic gases is not included in the model. Cloud water chemistry is included in the model to simulate the aqueous formation of SO_4^{2-} from the oxidation of S(IV) by hydrogen peroxide, O_3, trace metals (e.g., iron), and radical species

(Fahey and Pandis, 2001). The Fahey and Pandis (2001) mechanism also produces HCOOH from the aqueous oxidation of formaldehyde. No cloud SOA chemistry is included in these simulations, but aerosol chemistry as described by Knote et al., 2014 is represented. . Both aerosol-radiation (with aerosol optical properties based on the volume approximation) and aerosol-cloud interactions are included in the simulation (Chapman et al., 2009).

Emissions are from several sources. Anthropogenic emissions are from the EPA's National Emissions Inventory from 2017 combined with the CAMS global emissions inventory to include emissions from central Canada and shipping emissions. Biogenic emissions are calculated during the model simulation using the Model of Emissions of Gases and Aerosols from Nature (MEGAN) v2.0.4 (Guenther et al., 2006), which are adjusted for local shortwave radiation, and temperature conditions as predicted by WRF-Chem. Fire emissions are from the Fire Inventory from NCAR v1.6 (Wiedinmyer et al., 2011).

Configuration of WRF-Chem simulations

Parameter	Value
Simulation Period	06/27/2018 0:00 UTC - 07/2/2018 12:00 UTC
Meteorology Initial and Boundary Conditions	GFS Final Analysis
Horizontal Resolution	12kmx12km
Grid Points (x,y,z)	501x333x43
Microphysics	Morrison two-moment scheme
Short/Longwave radiation	Rapid Radiative Transfer Model
Land-surface	Noah Unified Land Surface Model
Boundary Layer	Yonsei University
Cumulus Scheme	Grell-Freitas
Chemical and Initial Boundary Conditions	Whole Atmosphere Community Climate Model
Chemistry and Aerosol Schemes	MOZART-MOSAIC with Cloud Chemistry
Biogenic Emissions	MEGANv 2.0.4
Anthropogenic Emissions	CAMS 2018 combined with 2017 EPA National Emissions Inventory
Wildfire Emissions	FINNv 1.6

Cloud LWC and Temperature
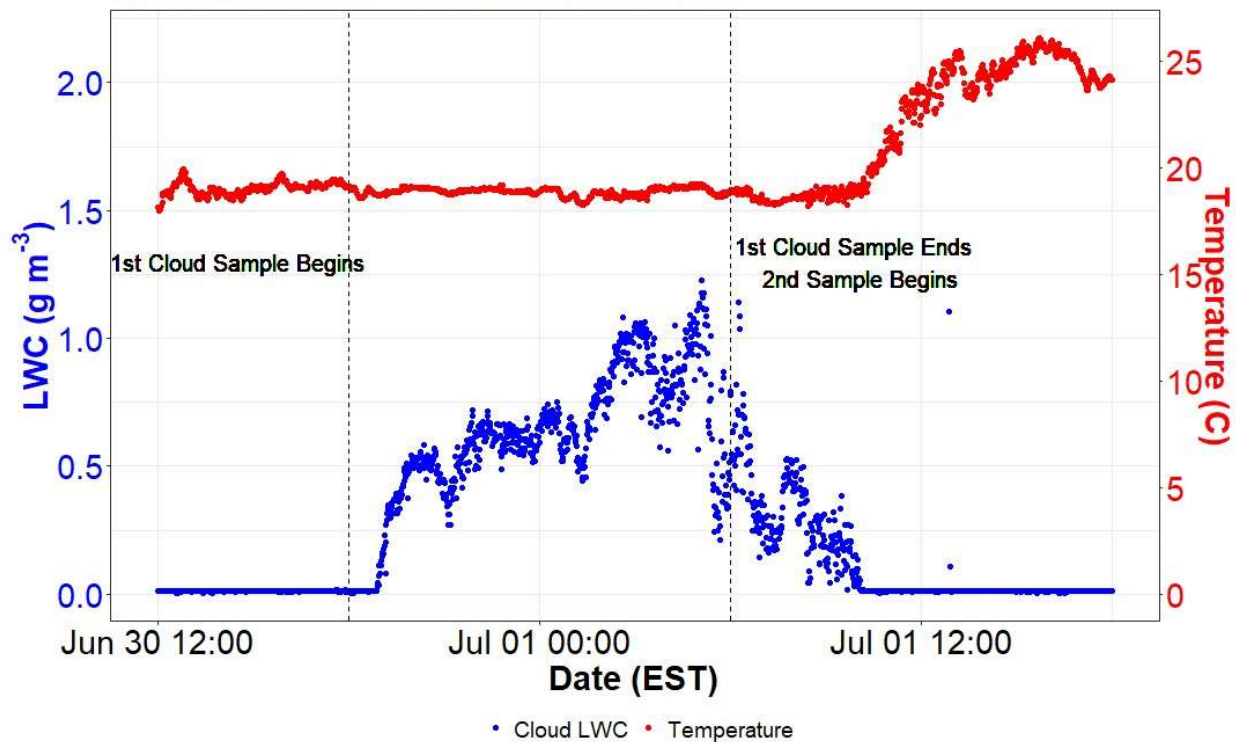### 06/30/2018 12:00 - 07/01/2018 12:00 EST

Figure S4. Time series (in EST) of cloud liquid water content (blue) measured in g m^{-3} and temperature (red) measured at the summit of WFM before and during the pollution event.

Table S1. Values used to determine gas phase organic acid mixing ratios at 298.15K

Organic Acid	Ka$_1$	Ka$_2$	K$_H$	ΔH$_s$/R
HCOOH	$1.82x10^{-4}$	NA	8800	6100 K
CH$_3$COOH	$1.78x10^{-5}$	NA	4053	6200 K
OxAc	0.056	$5.62x10^{-5}$	$6.18x10^8$	NA**

** The Sander et 2023 recommended K$_H$ value provides no enthalpy value for oxalic acid.

Section S4. Heat Wave During the Pollution Event
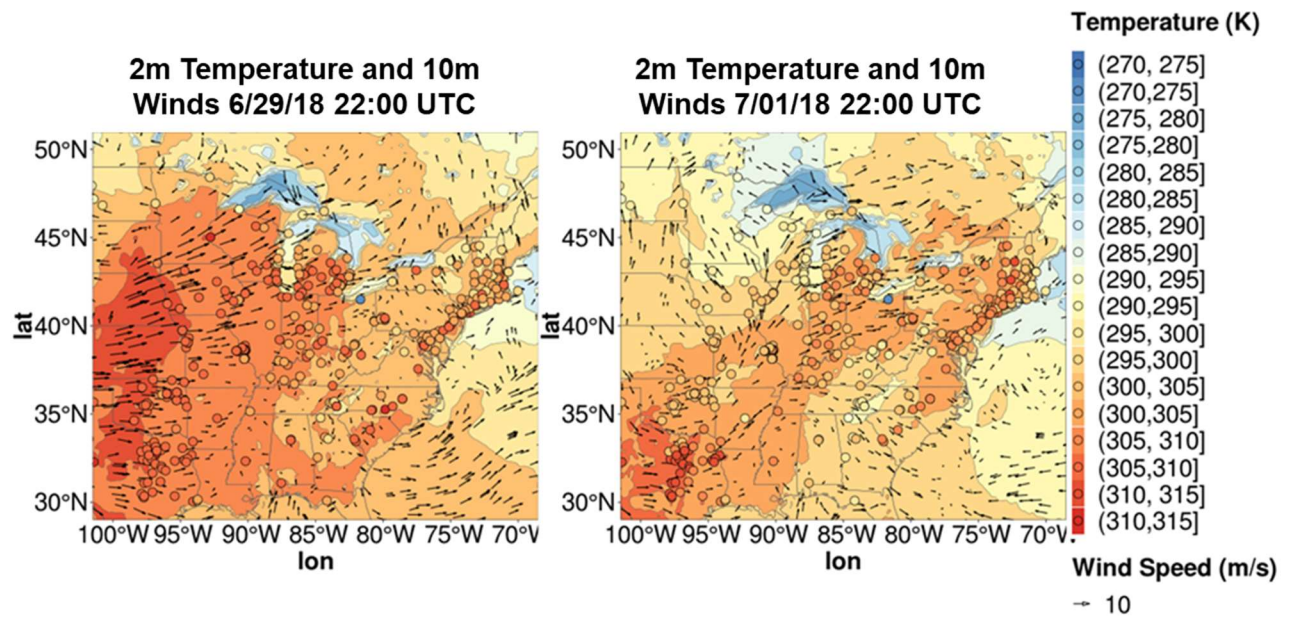
Figure S5. WRF-Chem simulated 2-meter temperature and 10m winds for a) 06/28/18 and b) 07/01/2018 at 22:00 UTC. Points represent temperature measurements collected from the EPA's AQS Monitoring Program
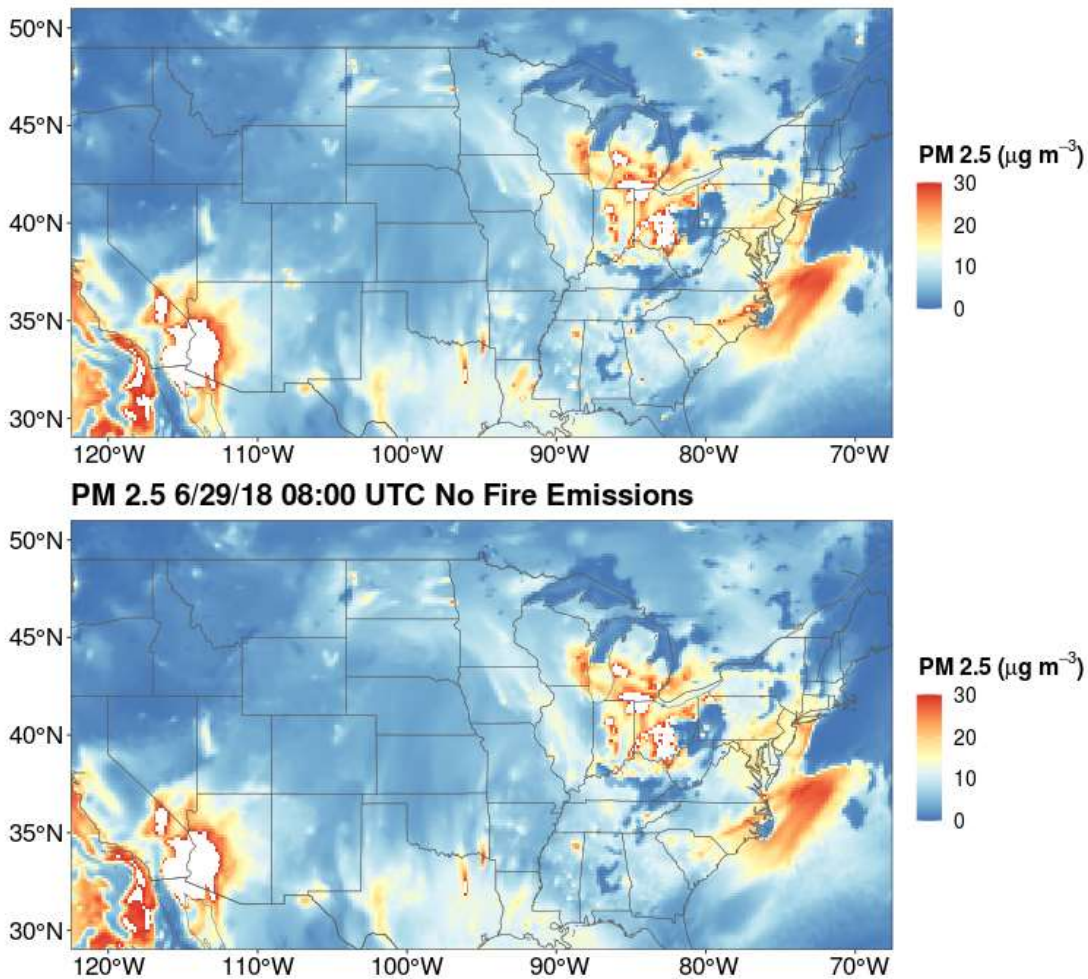
Section S5. Results With and Without Wildfire Emissions

Figure S6. Simulated PM 2.5 concentrations on 6/29/2018 08:00 UTC from WRF-Chem a) with fire emissions and b) no fire emissions.

Section S6. WRF-Chem Time Series Performance

Figures S8 shows a comparison between WRF-Chem simulations and measurements of O_3, PM 2.5, and 2m temperature made at the base of WFM, Pinnacle State Park, and Queens College. More information about the measurement sites can be found in Brandt et al., 2016 and Ninneman et al., 2020. At WFM, WRF-Chem struggles to model O_3, and 2m temperature at WFM, but performs well in predicting PM 2.5. The 12x12km horizontal grid resolution may not be fine enough to properly represent the complex geography of WFM, and therefore may not capture the meteorological processes properly. The uncertainties surrounding cloud cover, planetary boundary layer height, and temperature then may lead to the uncertainties surrounding O_3. At PSP, the 2-m temperature is well captured, especially after the first day (spin-up) of simulation, likely because of the OBSGRID nudging used in the simulation. After June 27, the magnitude of O_3 and PM2.5 is well captured as O_3

is within 5 ppbv and PM2.5 is within 5 ug/m3 for most of the simulation. Discrepancies in PM2.5 may be due to WRF-Chem underpredicting the PBLH at nighttime and thus concentrating the PM2.5 into a smaller volume than what actually occurred. At the Queens College urban site, both 2-m temperature and O3 show good agreement between WRF-Chem and observations. However, while the increasing trend over the pollution event is well captured, PM2.5 concentrations are overpredicted by 20 ug/m3 or more, which may be caused by an over-prediction of aerosol emissions (or their precursor gases) and/or PBLH prediction.
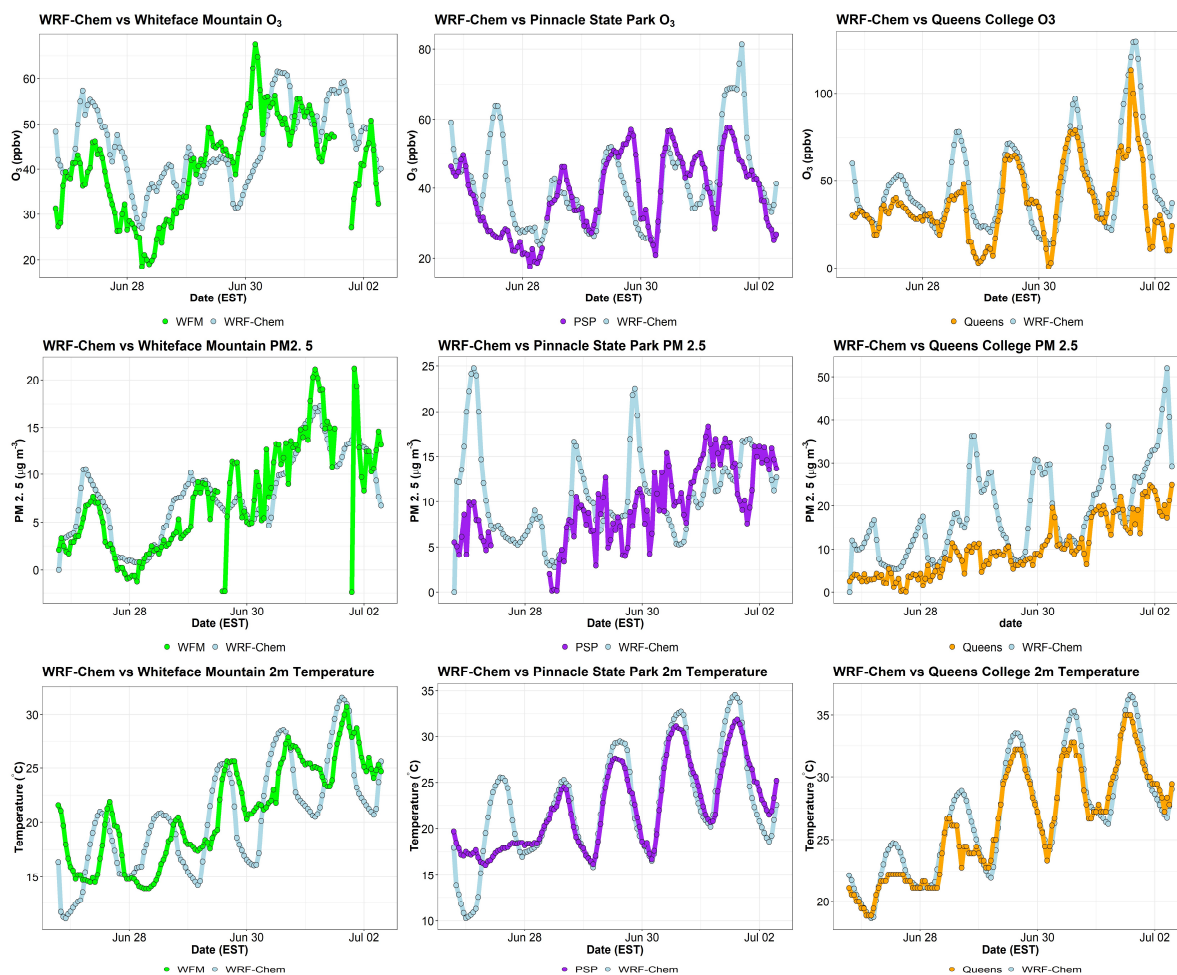
Figure S7. WRF-Chem performance for surface O3, surface PM 2.5, and 2m temperature for WFM, Pinnacle State Park, and Queens College, NY.

Section S7. Simulating Dilution in BOXMOX Simulations

Entrainment of background air into an air parcel during Lagrangian box modeling can have important impacts on mixing ratios of gas species, particularly for simulations with atmospheric chemical lifetimes longer than a few hours. Therefore, careful consideration must be made when choosing parameters for dilution. Dilution is calculated within BOXMOX using a parameterization of the continuity equation:

$$\frac{\partial c_i}{\partial t} = K_{turb}(c_i - c_{ibg})$$

Where c_i is the mixing ratio of species i, c_{ibg} is the background mixing ratio of species i, and K_{turb} is the first order dilution rate constant. Sensitivity studies were conducted to estimate the uncertainty associated with different values of K_{turb}. In these simulations, K_{turb} was set to 5 values associated with dilution times of 6, 12, 24, and 48 hours, and a simulation that included zero entrainment of background air. To simplify the analysis, only one trajectory was used for the simulations. Figure S9 shows the results of the dilution sensitivity analysis for all 5 K_{turb} values, and the associated background mixing ratios for HCOOH and CH_3COOH. The dilution parameter does have significant impacts on organic acid mixing ratios, as the background mixing ratios are up to ten times less than the mixing ratios within the box model. Despite the large spread in organic acid mixing ratios, the overall conclusions of the work were not impacted by the selection of K_{turb}. We chose a K_{turb} value $(1.17 \times 10^{-5}\ s^{-1})$ that gives a 24-hour dilution time for all BOXMOX modeling simulations.
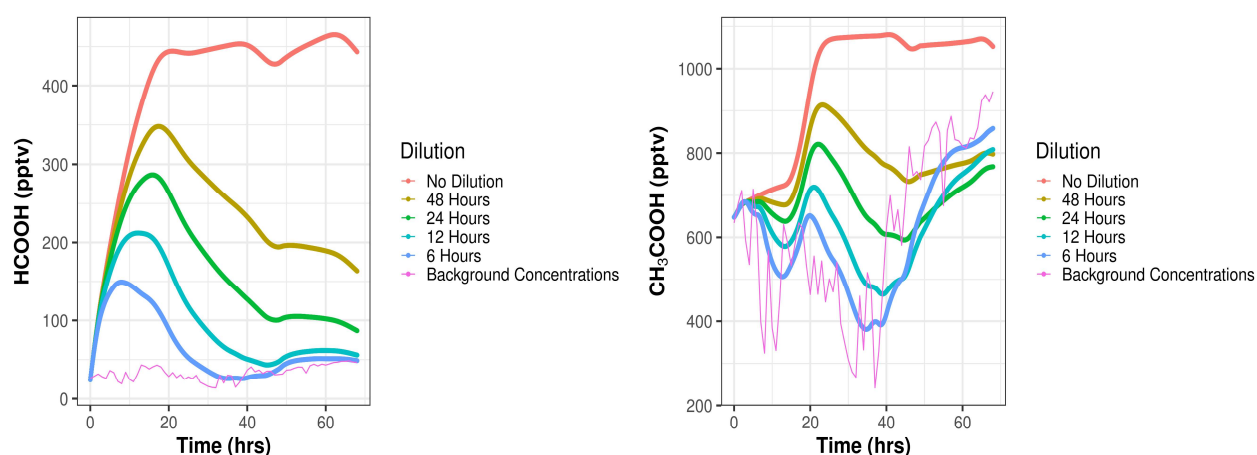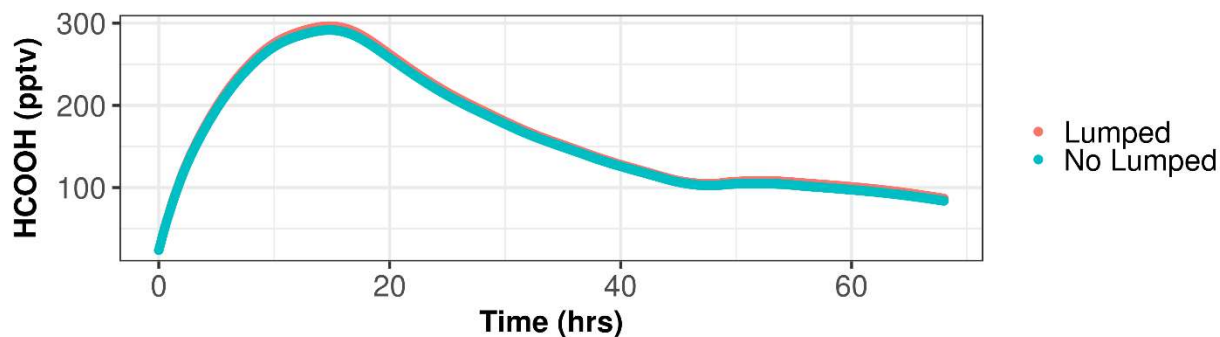

Figure S8. Results of sensitivity analysis of K_{turb} for a) HCOOH and b) CH3COOH. Lines are colored by the dilution time associated with the K_{turb} value. The magenta line represents the background mixing ratios used for entrainment.

Section S8. Bulk Species Sensitivity Study

HCOOH With and Without Lumped Species in MCMv 3.3.1

CH$_3$COOH With and Without Lumped Species in MCMv 3.3.1
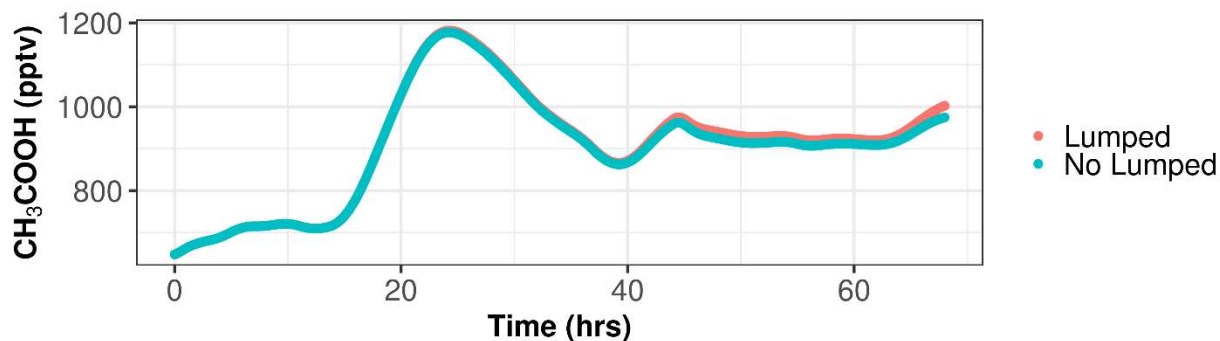
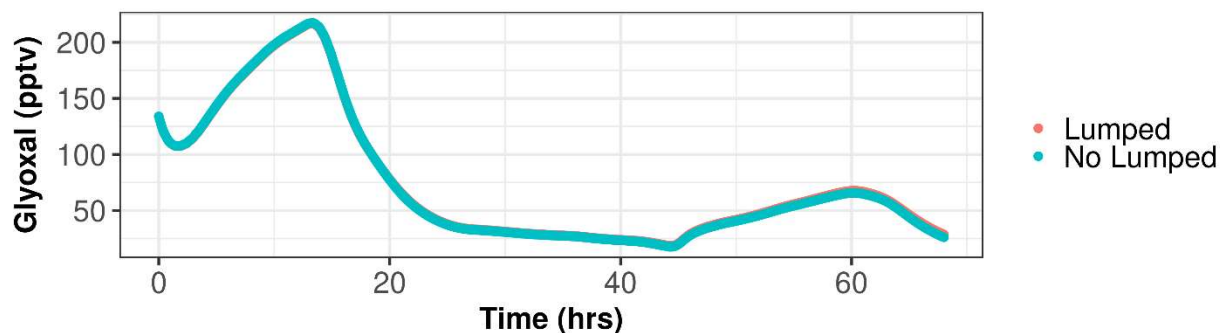### Glyoxal With and Without Lumped Species in MCMv 3.3.1

Figure S9. Sensitivity of HCOOH, CH$_3$COOH and Glyoxal in MCMv 3.3.1 by setting the initial conditions and emissions of the MOZART T1 lumped species BIGALK, BIGENE, and XYLENES to 0.
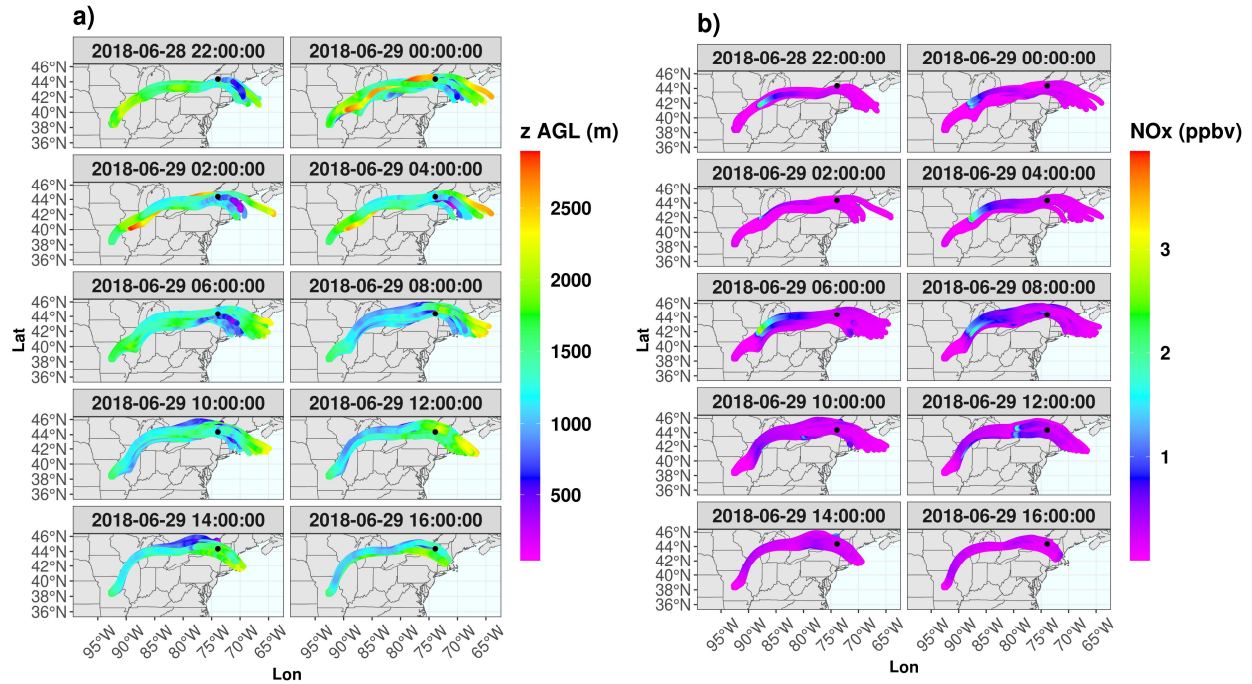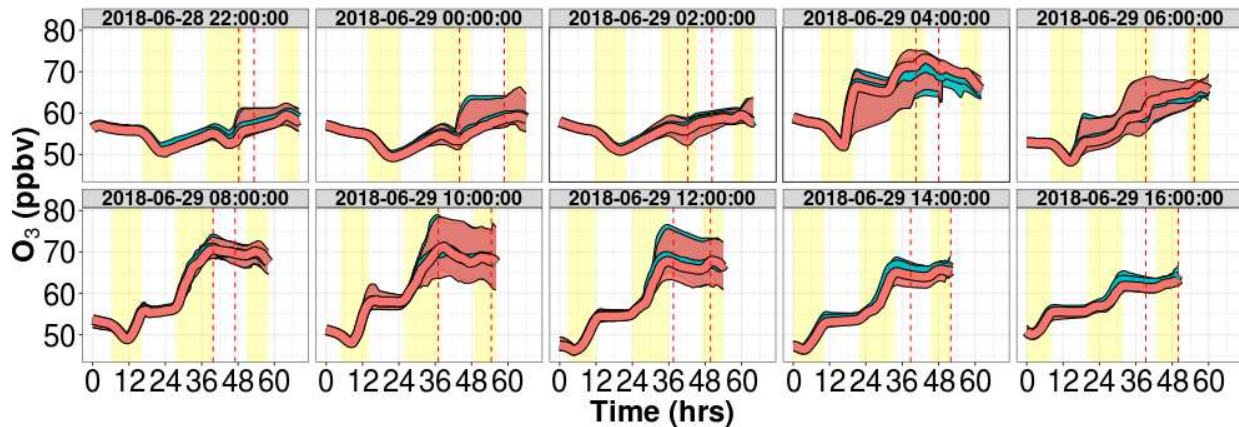
Section S9. Full Trajectory Ensemble Results

Figure S10. WRF-Chem forward trajectory ensemble results for: a) trajectory height AGL in meters and b) NO$_x$ mixing ratios in ppbv.

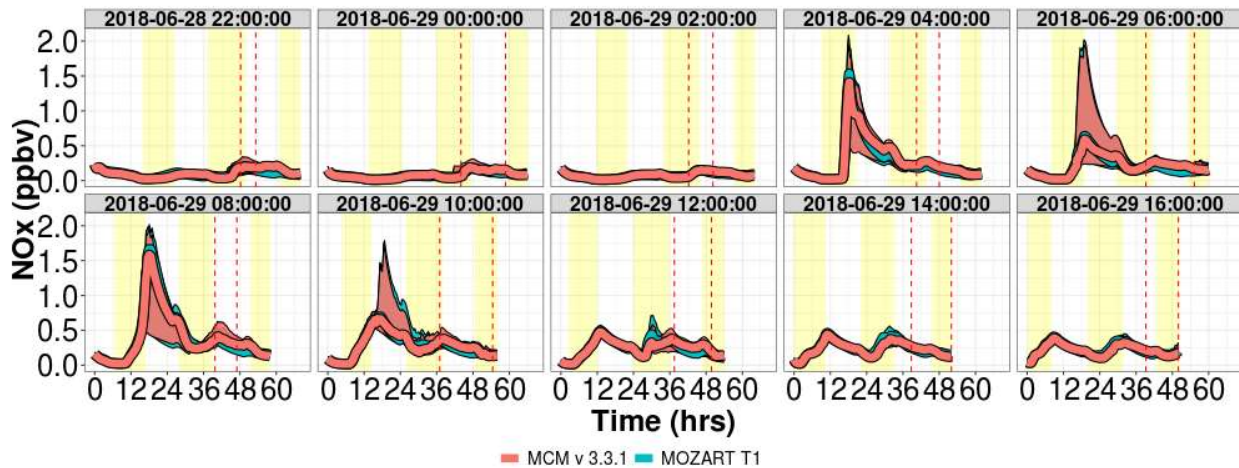## Section S10. O$_3$ and NO$_x$ Mixing Ratios

Figure S11. Averaged time series of O_3 and NO_x mixing ratios for MOZART T1 (blue) and MCMv 3.3.1 (red) for the WRF-Chem forward trajectory ensembles, separated by launch date. Lines represent the median value for the ensemble with the shading represents the interquartile range.

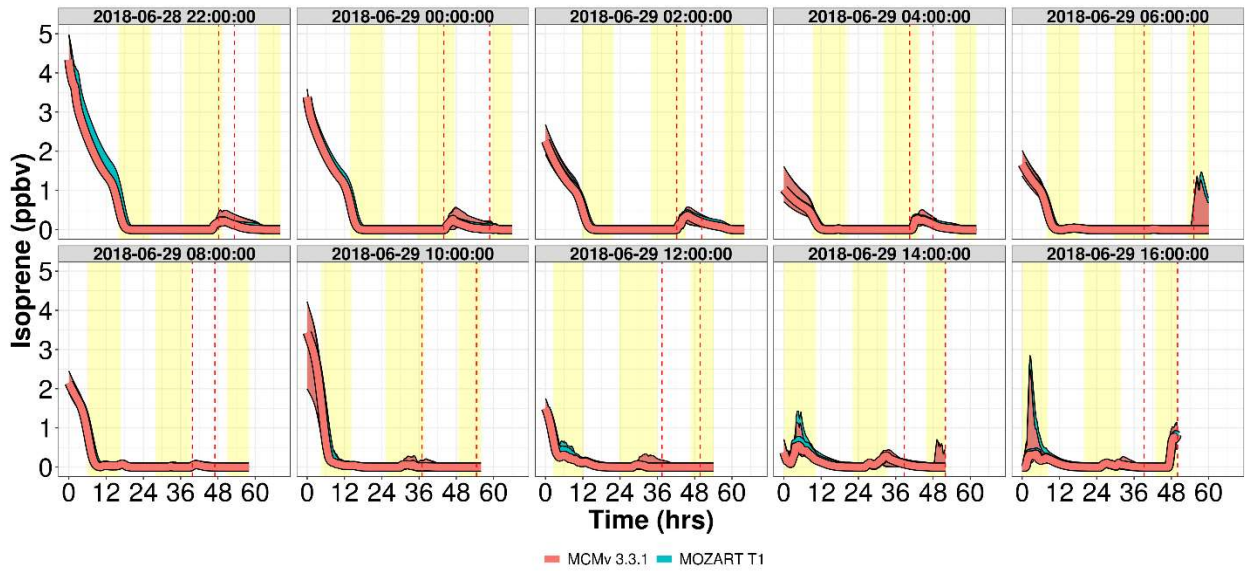## Isoprene MCMv 3.3.1 vs MOZART T1

Figure S12. Averaged time series of isoprene mixing ratios for MOZART T1 (blue) and MCMv 3.3.1 (red) for the WRF-Chem forward trajectory ensembles, separated by launch date. Lines represent the median value for the ensemble with the shading represents the interquartile range.
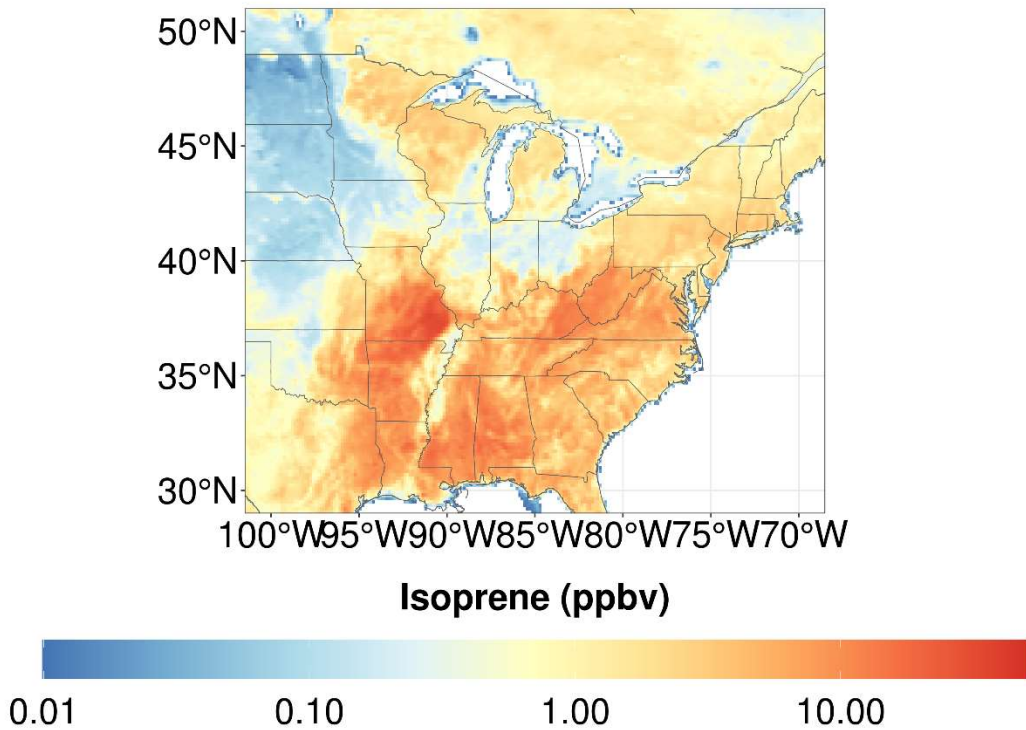
Figure S13. WRF-Chem simulated isoprene mixing ratios for 6/29/2018 20:00 UTC.

Section S11. Formic Acid Production

Figure S14 shows the production pathways of HCOOH between MOZART T1 and MCMv 3.3.1. The total production of HCOOH is in strong agreement between the two mechanisms, with the ozonolysis of isoprene and isoprene oxidation products MACR and MVK producing the vast majority of HCOOH, though in slightly different yields.
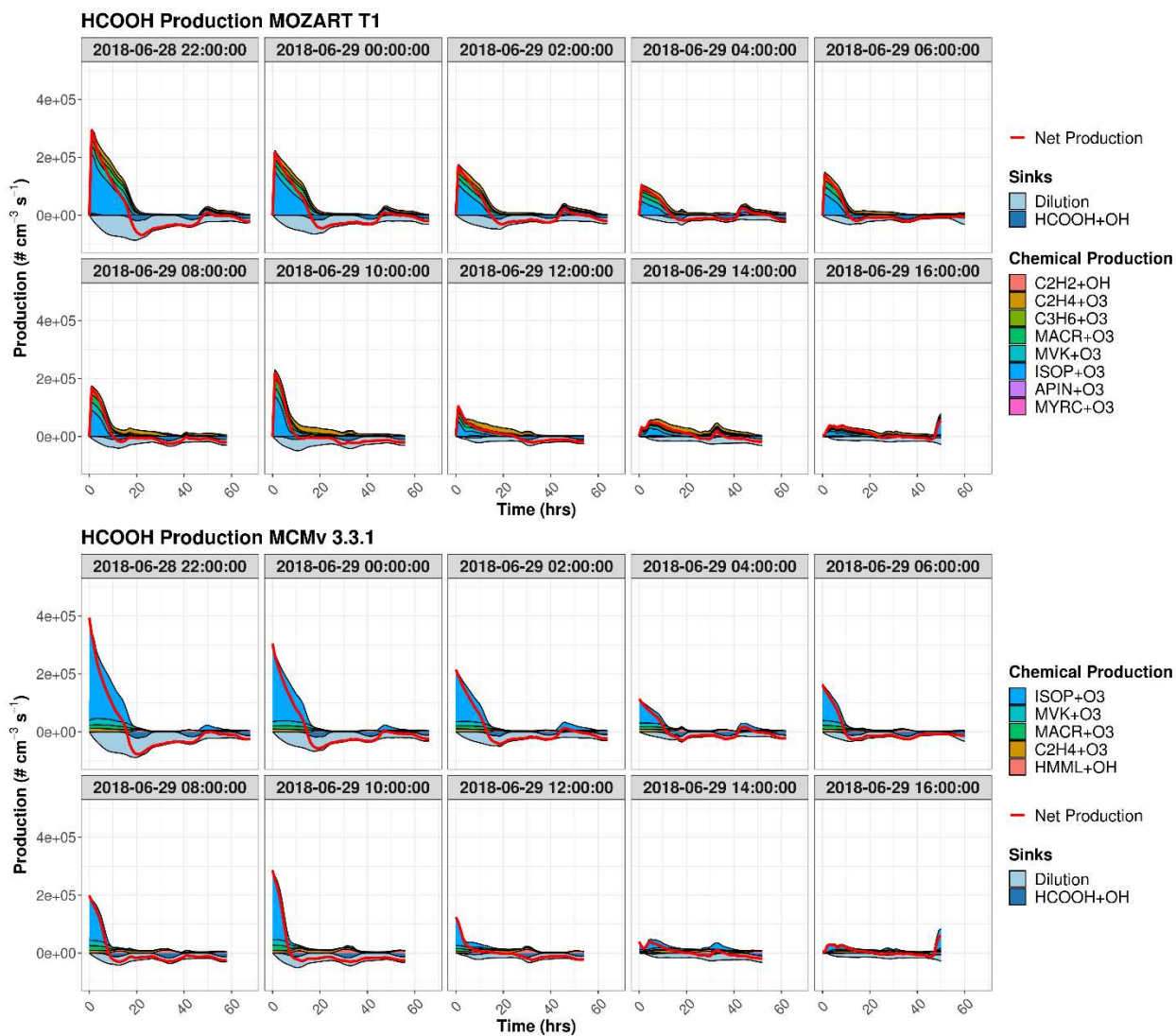

Figure S14. Chemical sources, sinks, and net production (red line) of HCOOH for a) MOZART T1 and MCMv 3.3.1, separated by trajectory launch date. The red line shows the overall net production rates of HCOOH.
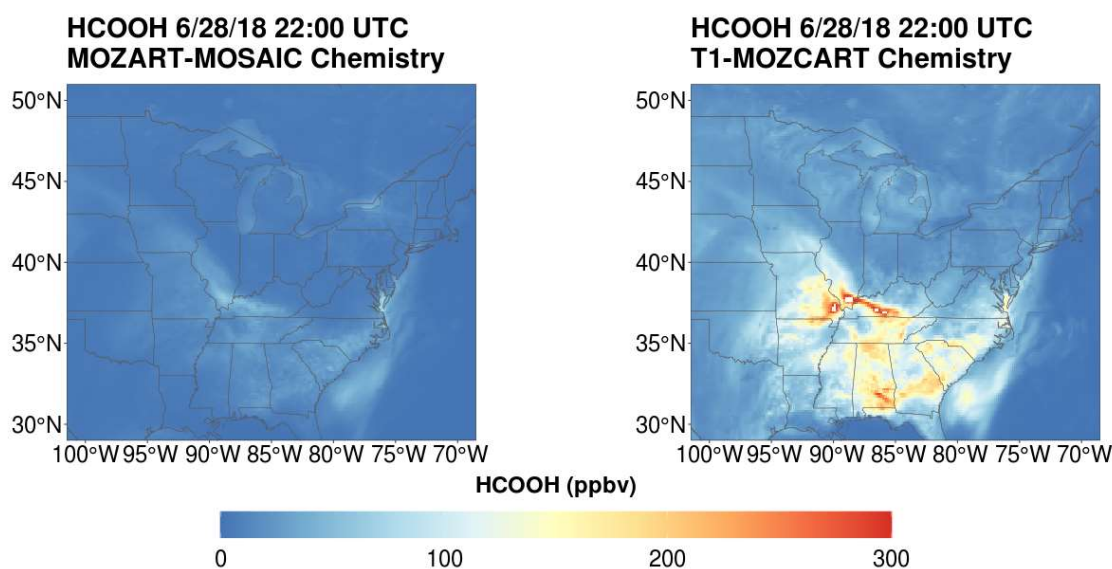
Figure S15. Simulated HCOOH mixing ratios on 6/28/2018 22:00 UTC from WRF-Chem using the a) MOZART-MOSAIC chemistry mechanism and b) T1-MOZCART chemistry mechanism.

Section S12. Acetic Acid Production

MCM shows stronger production of CH_3COOH under conditions of high isoprene mixing ratios and low NO_x mixing ratios, such as trajectories launched on 6/28/2018 22:00 UTC and 6/29/2018 at 0:00 UTC (see Figures S12). Further investigation of the production rates reveals MCM predicts stronger production from the reaction of the acetyl peroxy radical (CH_3CO_3) with the hydroperoxy radical (HO_2) and to a lesser extent, from CH_3CO_3+organic peroxy (RO_2) reactions.
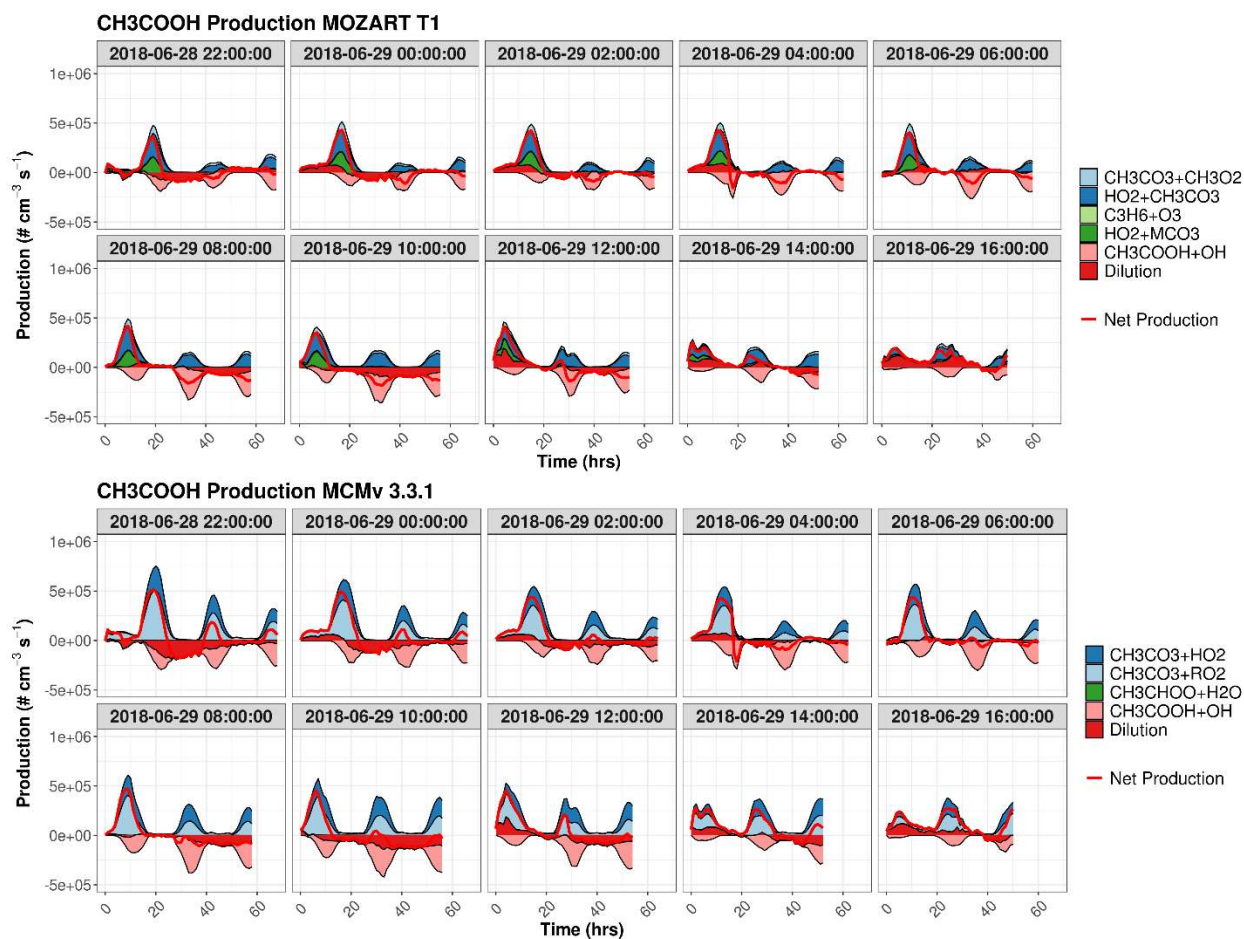
Figure S16. Chemical sources, sinks, and net production (red line) of CH_3COOH for MOZART T1 and MCMv 3.3.1, separated by trajectory launch date. The red line shows the overall net production rates of CH_3COOH.

Figure S17 shows the times series of CH_3CO_3 mixing ratios for MOZART T1 and MCM, while Figure S18 and Figurs S19 show the reactivity and production rates of CH_3CO_3 for both MOZART T1 and MCM. MCM exhibits up to 750 pptv greater mixing ratios in low NO_x/high isoprene scenarios compared to MOZART T1, while it exhibits similar mixing ratios in the presence of higher NO_x. The underlying chemistry leading to the discrepancies between the two mechanisms occurs for several reasons. First, the removal of CH_3CO_3 by RO_2 (represented by CH_3O_2, MCO_3, $MACRO_2$, $ISOPAO_2$, $ISOBAO_2$, $ISOPNO_3$, and XO_2 in MOZART T1) in the first 20 hours of the simulations is stronger compared to species in MCM (which are represented by the sum of all RO_2 species within the mechanism). However, the yield of CH_3COOH from reaction with RO_2 is greater in MCMv 3.3.1 compared to MOZART T1, offsetting this greater reactivity. Second, CH_3CO_3 mixing ratios are up to 2.5x greater in the second half of the simulations due to greater production from methylglyoxal from both reaction with OH and from photolysis. This is driven by the greater methylglyoxal production within MCM compared to MOZART T1. Finally, there is a greater formation from peracetic acid (CH_3CO_3H). CH_3CO_3H is not a direct chemical source of CH_3CO_3 but rather a chemical reservoir of CH_3CO_3 via its reaction with HO_2 which can then be reversed

by reacting with OH. However, the rate constant of CH_3CO_3H+OH in MCM is 3.7 times faster than the equivalent rate constant in MOZART T1, leading to a greater fraction of CH_3CO_3 compared to CH_3CO_3H in MCM. There is evidence that this reaction rate is overestimated in both mechanisms, making CH_3CO_3H a less permanent chemical sink in both models compared to observations (Berasategui et al., 2020)
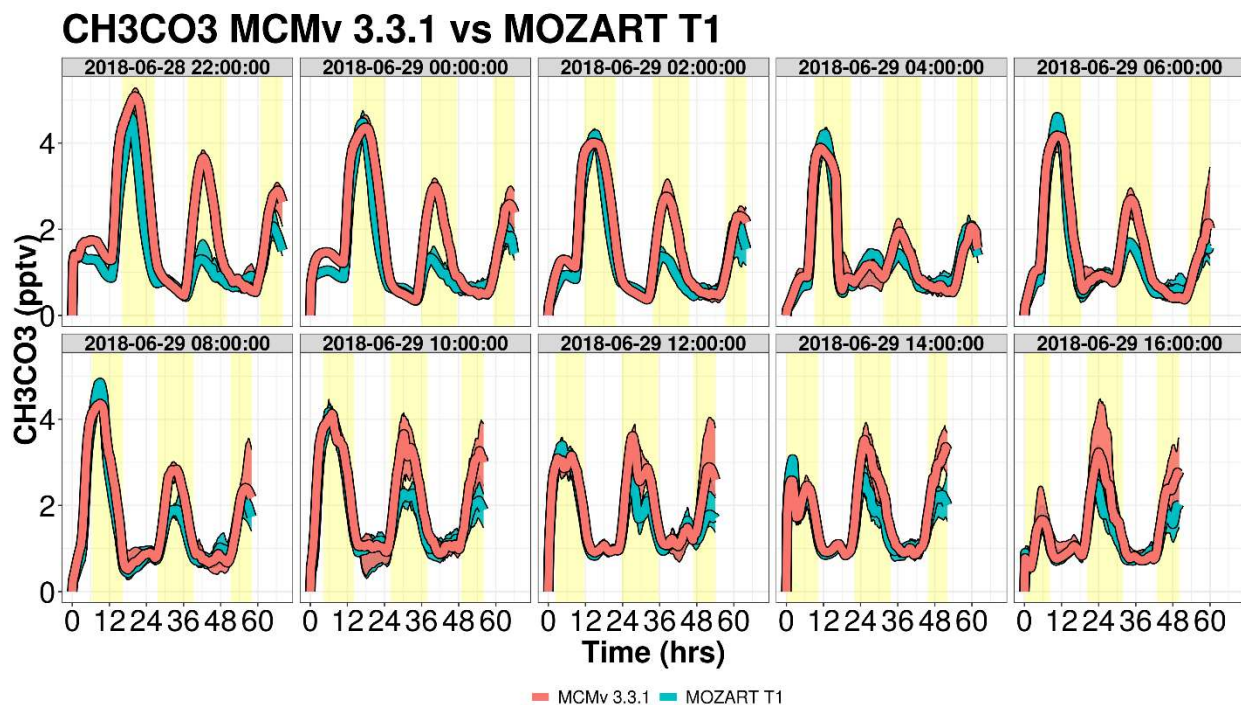

Figure S17. Averaged time series of CH_3CO_3 mixing ratios for Mozart T1 (blue) and MCM (red) for the WRF-Chem forward trajectory ensembles, separated by launch date. Lines represent the median value for the ensemble with the shading represents the interquartile range.
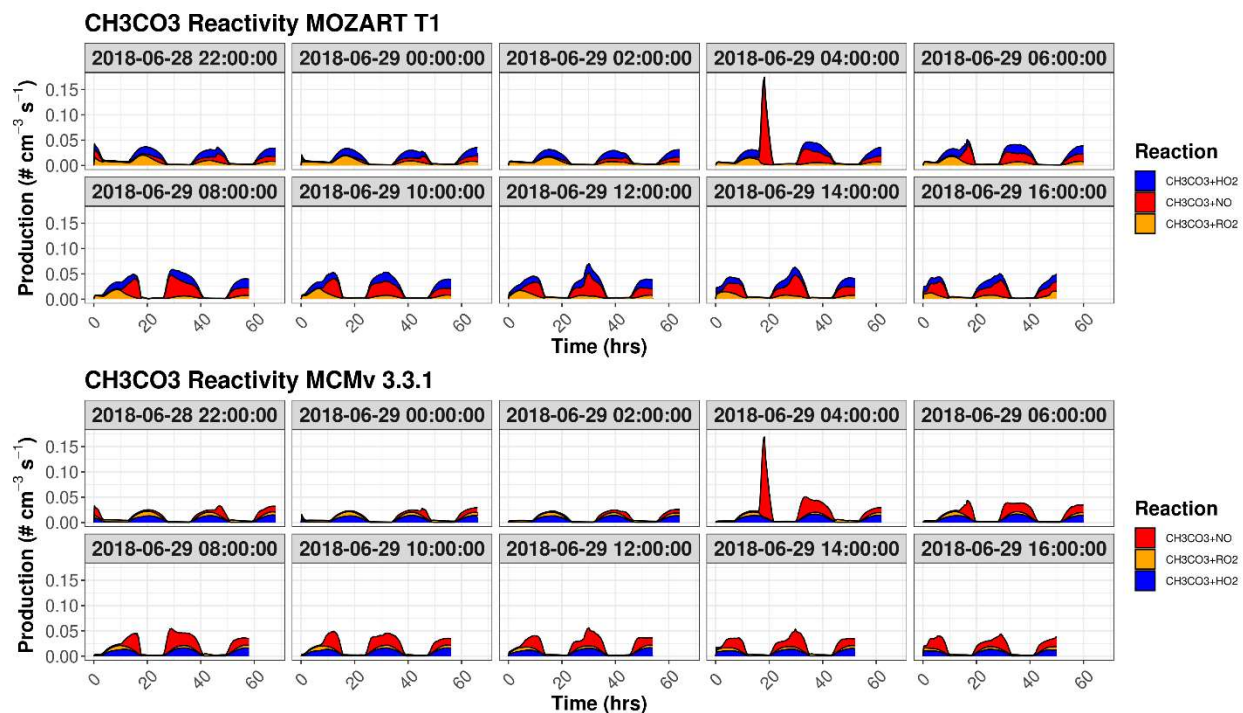
Figure S18. Chemical reactivity of CH₃CO₃ for MOZART T1 and MCMv 3.3.1, separated by trajectory launch date.
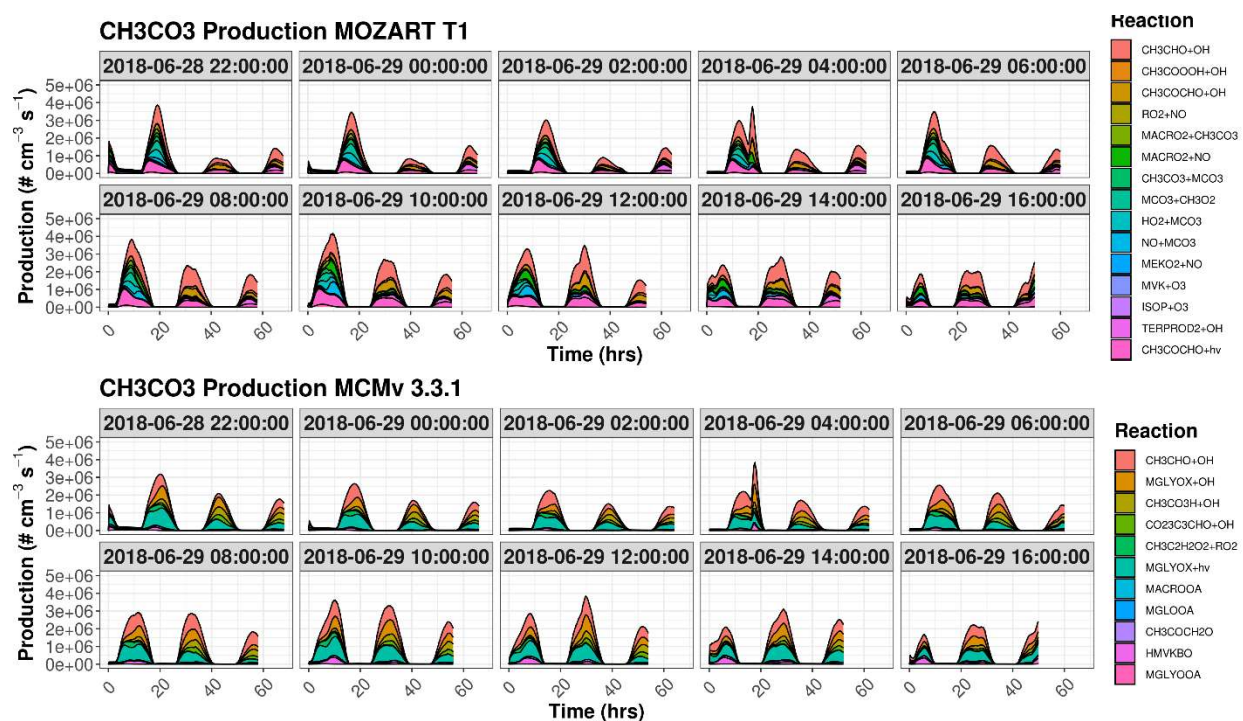

Figure S19. Chemical production pathways for CH₃CO₃ for MOZART T1 and MCMv 3.3.1, separated by trajectory launch date.

Section S13. Glyoxal Production

The differences in glyoxal production between MOZART T1 and MCMv 3.3.1 are multifaceted. There is a strong nighttime production from ozonolysis reactions of low NO_x isoprene oxidation products such as isoprene hydroperoxyl aldehydes (C5HPALD2) and PGAOOB (an ozonolysis product of C5HPALD2). During the daytime under low NO_x conditions, the production rates are relatively similar, but as trajectories fly over the Chicago metropolitan area and are influenced by high NO_x emissions, MOZART shows up to 2x greater glyoxal production vs MCMv 3.3.1, via the XO_2+NO pathway. XO_2 is a lumped organic peroxy radical species representing oxygenated isoprene compounds including isoprene unsaturated hydroperoxides, isoprene epoxydiols, and isoprene unsaturated hydroperoxyaldehydes. It is possible that the simplification of this chemistry could lead to an over-prediction of the production of glyoxal under high NO_x conditions.
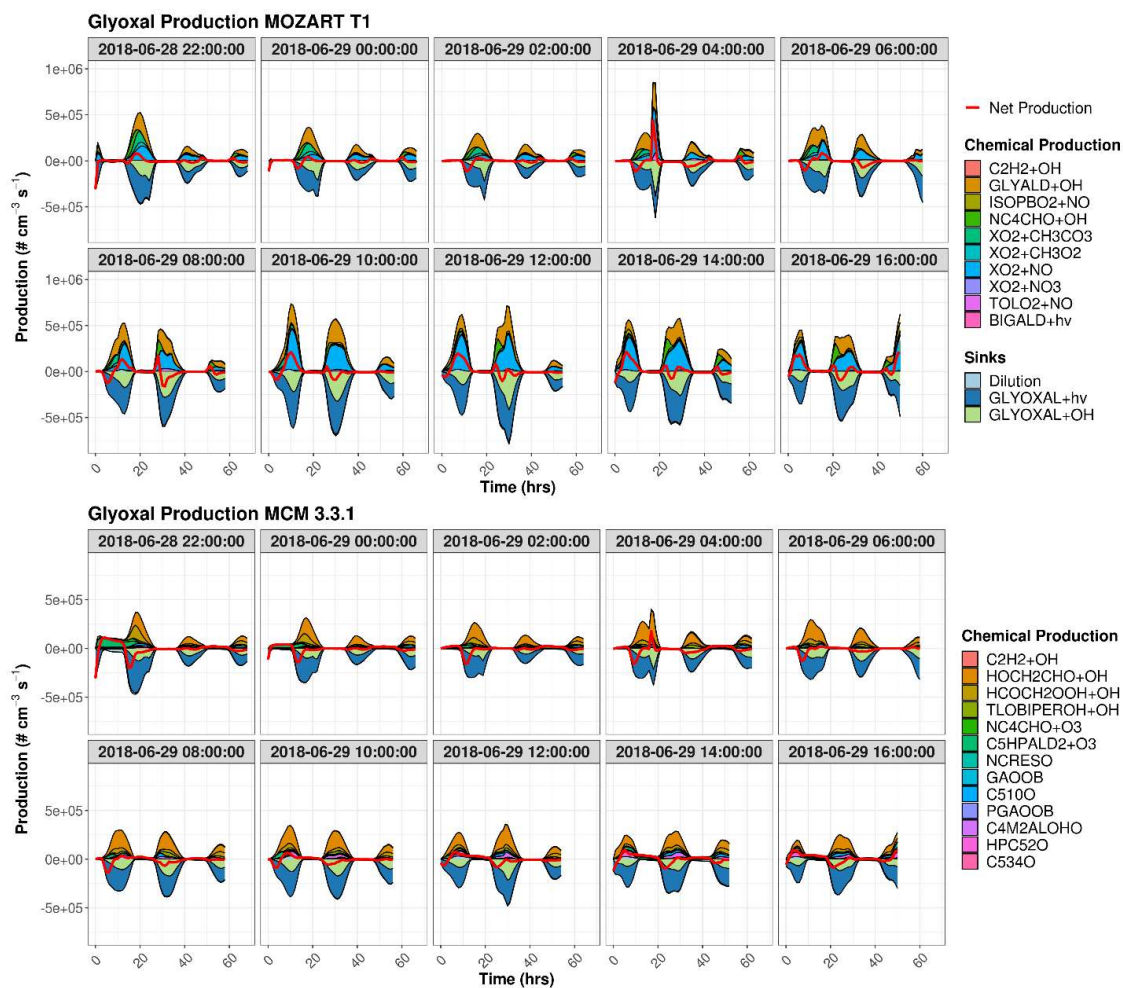

Figure S20. Chemical production pathways for glyoxal for MOZART T1 and MCMv 3.3.1, separated by trajectory launched date. The red line shows the overall net production rates of glyoxal.
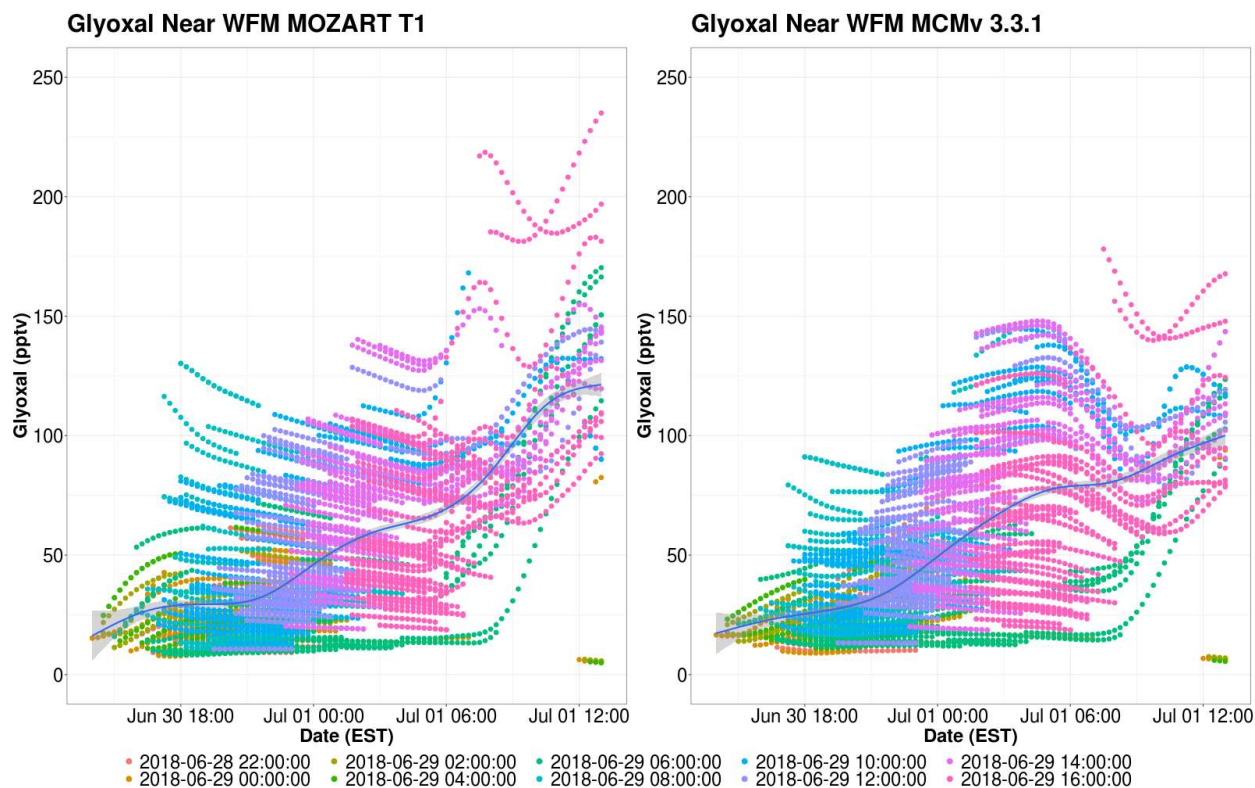
Figure S21. Glyoxal mixing ratios with 1° latitude and longitude of WFM from MOZART T1 and MCM. The smoothed trendline is calculated using a generalized additive model.

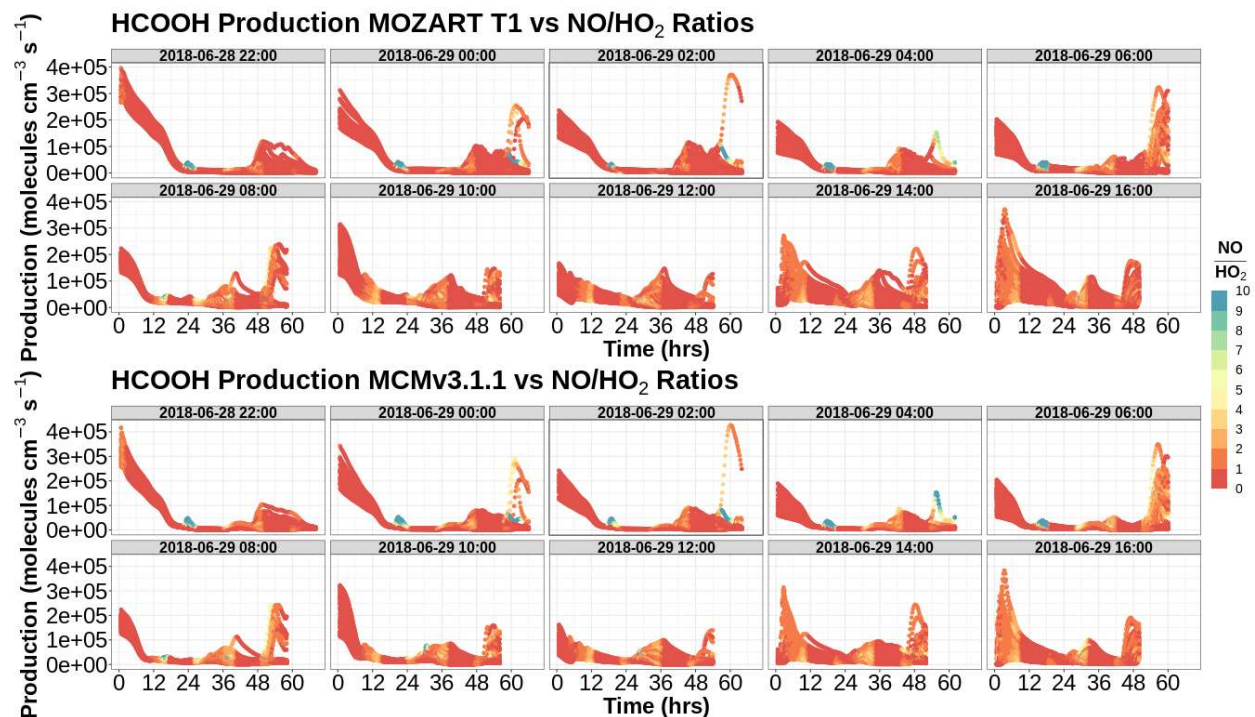## Section S14. Anthropogenic Influences on Organic Acid Formation

Figure S22. Time series of the production of HCOOH colored by NO/HO₂ ratios, separated by trajectory start date
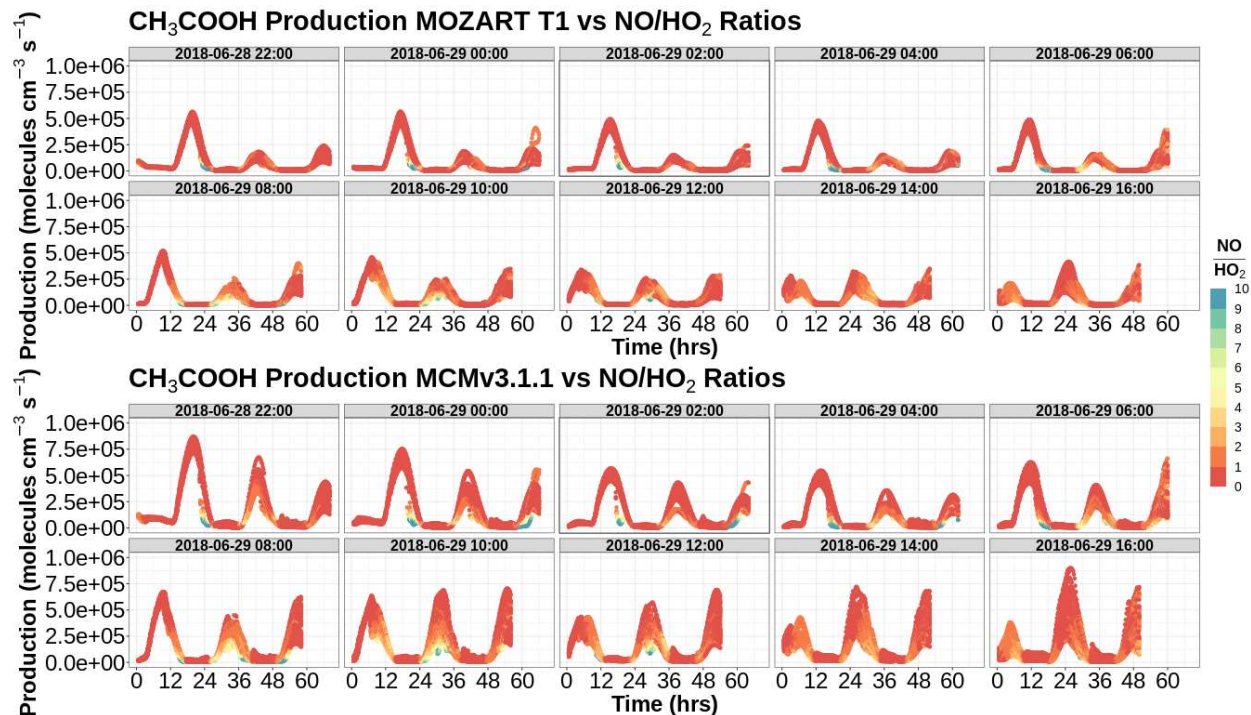

Figure S23. Time series of the production of CH₃COOH colored by NO/HO₂ ratios, separated by trajectory start date
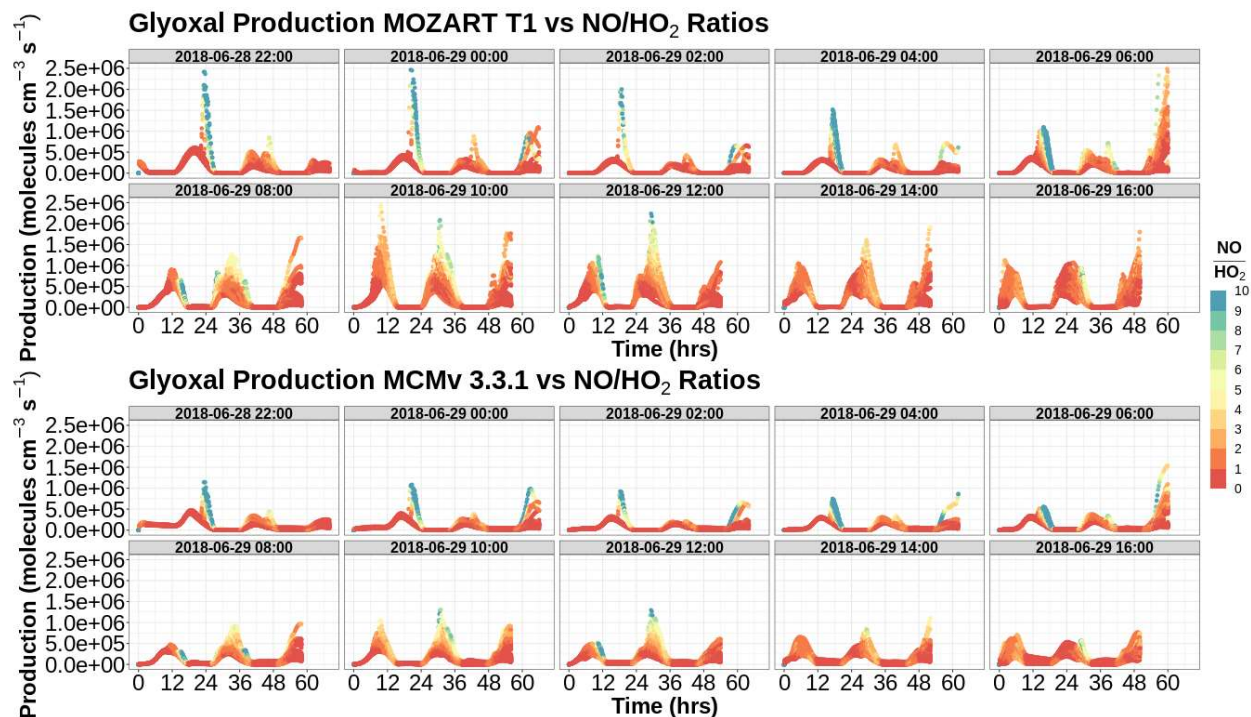
Figure S24. Time series of the production of glyoxal colored by NO/HO$_2$ ratios, separated by trajectory start date

References

Berasategui, M., Amedro, D., Vereecken, L., Lelieveld, J., and Crowley, J. N.: Reaction between CH$_3$C(O)OOH (peracetic acid) and OH in the gas phase: a combined experimental and theoretical study of the kinetics and mechanism, Atmospheric Chem. Phys., 20, 13541–13555, https://doi.org/10.5194/acp-20-13541-2020, 2020.

Brandt, R. E., Schwab, J. J., Casson, P. W., Roychowdhury, U. K., Wolfe, D., Demerjian, K. L., Civerolo, K. L., Rattigan, O. V., and Felton, H. D.: Atmospheric Chemistry Measurements at Whiteface Mountain, NY: Ozone and Reactive Trace Gases, Aerosol Air Qual. Res., 16, 873–884, https://doi.org/10.4209/aaqr.2015.05.0376, 2016.

Chapman, E. G., Gustafson, W. I. J., Easter, R. C., Barnard, J. C., Ghan, S. J., Pekour, M. S., and Fast, J. D.: Coupling aerosol-cloud-radiative processes in the WRF-Chem model: Investigating the radiative impact of elevated point sources, Atmospheric Chem. Phys., 9, 945–964, https://doi.org/10.5194/acp-9-945-2009, 2009.

Emmons, L. K., Walters, S., Hess, P. G., Lamarque, J.-F., Pfister, G. G., Fillmore, D., Granier, C., Guenther, A., Kinnison, D., Laepple, T., Orlando, J., Tie, X., Tyndall, G., Wiedinmyer, C., Baughcum, S. L., and Kloster, S.: Description and evaluation of the Model for Ozone and Related chemical Tracers, version 4 (MOZART-4), Geosci. Model Dev., 3, 43–67, https://doi.org/10.5194/gmd-3-43-2010, 2010.

Fahey, K. M. and Pandis, S. N.: Optimizing model performance: variable size resolution in cloud chemistry modeling, Atmos. Environ., 35, 4471–4478, https://doi.org/10.1016/S1352-2310(01)00224-2, 2001.

Fast, J. D., Gustafson Jr., W. I., Easter, R. C., Zaveri, R. A., Barnard, J. C., Chapman, E. G., Grell, G. A., and Peckham, S. E.: Evolution of ozone, particulates, and aerosol direct radiative forcing in the vicinity of Houston using a fully coupled meteorology-chemistry-aerosol model, J. Geophys. Res. Atmospheres, 111, https://doi.org/10.1029/2005JD006721, 2006.

Grell, G. A., Peckham, S. E., Schmitz, R., McKeen, S. A., Frost, G., Skamarock, W. C., and Eder, B.: Fully coupled "online" chemistry within the WRF model, Atmos. Environ., 39, 6957–6975, https://doi.org/10.1016/j.atmosenv.2005.04.027, 2005.

Guenther, A., Karl, T., Harley, P., Wiedinmyer, C., Palmer, P. I., and Geron, C.: Estimates of global terrestrial isoprene emissions using MEGAN (Model of Emissions of Gases and Aerosols from Nature), Atmospheric Chem. Phys., 6, 3181–3210, https://doi.org/10.5194/acp-6-3181-2006, 2006.

Knote, C., Hodzic, A., Jimenez, J. L., Volkamer, R., Orlando, J. J., Baidar, S., Brioude, J., Fast, J., Gentner, D. R., Goldstein, A. H., Hayes, P. L., Knighton, W. B., Oetjen, H., Setyan, A., Stark, H., Thalman, R., Tyndall, G., Washenfelder, R., Waxman, E., and Zhang, Q.: Simulation of semi-explicit mechanisms of SOA formation from glyoxal in aerosol in a 3-D model, Atmospheric Chem. Phys., 14, 6213–6239, https://doi.org/10.5194/acp-14-6213-2014, 2014.

Lane, T. E., Donahue, N. M., and Pandis, S. N.: Simulating secondary organic aerosol formation using the volatility basis-set approach in a chemical transport model, Atmos. Environ., 42, 7439–7451, https://doi.org/10.1016/j.atmosenv.2008.06.026, 2008.

Ninneman, M., Lu, S., Zhou, X., and Schwab, J.: On the Importance of Surface-Enhanced Renoxification as an Oxides of Nitrogen Source in Rural and Urban New York State, ACS Earth Space Chem., 4, 1985–1992, https://doi.org/10.1021/acsearthspacechem.0c00185, 2020.

Sandu, A. and Sander, R.: Technical note: Simulating chemical systems in Fortran90 and Matlab with the Kinetic PreProcessor KPP-2.1, Atmospheric Chem. Phys., 6, 187–195, https://doi.org/10.5194/acp-6-187-2006, 2006.

Skamarock, C., Klemp, B., Dudhia, J., Gill, O., Liu, Z., Berner, J., Wang, W., Powers, G., Duda, G., Barker, D., and Huang, X.: A Description of the Advanced Research WRF Model Version 4.3, https://doi.org/10.5065/1dfh-6p97, 2021.

Wiedinmyer, C., Akagi, S. K., Yokelson, R. J., Emmons, L. K., Al-Saadi, J. A., Orlando, J. J., and Soja, A. J.: The Fire INventory from NCAR (FINN): a high resolution global model to estimate the emissions from open burning, Geosci. Model Dev., 4, 625–641, https://doi.org/10.5194/gmd-4-625-2011, 2011.

Zaveri, R. A., Easter, R. C., Fast, J. D., and Peters, L. K.: Model for Simulating Aerosol Interactions and Chemistry (MOSAIC), J. Geophys. Res. Atmospheres, 113, https://doi.org/10.1029/2007JD008782, 2008.